

Atomic Layer Deposition of Nanostructured Tunable Resistance Coatings: Growth, Characterization, and Electrical Properties

Anil U. Mane^a, William M. Tong^b, Alan D. Brodie^b,
Mark A. McCord^b, and Jeffrey W. Elam^a

^aArgonne National Laboratory, Argonne, Illinois 60439, USA

^bKLA-Tencor Corp., Milpitas, CA 95035, USA

We have developed atomic layer deposition (ALD) methods to synthesize robust nanostructured composite coatings with tunable resistance comprised of conducting, metallic nanoparticles embedded in an amorphous dielectric matrix. These films are nominally composed of M:Al₂O₃ where M= W or Mo, and are prepared using alternating exposures to trimethyl aluminum (TMA) and H₂O for Al₂O₃ ALD and alternating MF₆/Si₂H₆ exposures for the metal ALD. By varying the ratio of ALD cycles for the metal and Al₂O₃ components in the film, we can precisely adjust the resistivity of these composite coatings over a very broad range (e.g. 10¹²-10³ Ohm-cm). Furthermore, the self-limiting nature of ALD allows us to grow these nanocomposite films on a variety of complex substrates such as high aspect ratio porous 3D surfaces, MEMS devices, ceramics, grid structures and microchannel plates. Here we present a detailed ALD study of the nanostructured composite resistance coatings including in-situ material growth, microstructural characterization, and electrical measurements.

Introduction

Nanostructured composite thin film materials comprised of mixed conducting and insulating components have been utilized in a wide variety of applications including resistive layers for electron multipliers such as microchannel plates, resistive memories, electro-chromic devices, biomedical devices, and charge-dissipating coatings on micro-electromechanical systems (MEMS) devices and electron optics (1-6). By varying the precise composition of the mixture, the electrical, optical, and physical properties of the composite coatings can often be tuned over the full range of the individual components, and can sometimes yield unique properties distinct from either of the constituents. Amongst the various thin-film deposition processes, ALD is a technique for growing complex layers in a precisely controlled manner with many distinctive advantages (7). ALD is based on a binary sequence of self-limiting chemical reactions between precursor vapors and a solid surface. Because the two reactions in the binary sequence are performed separately, the gas phase precursors are never mixed and this eliminates the possibility of gas phase reactions that can form particulate contaminants and cause non-self-limiting chemical vapor deposition. This strategy yields monolayer-level thickness and composition control. The self-limiting aspect of ALD leads to continuous pinhole-free films, excellent step coverage, and conformal deposition on very high aspect ratio structures. This self-limiting property, coupled with facile diffusion of the precursor vapors into high aspect ratio narrow pores, vias, trenches and voids, allows complex 3D structures to be coated with excellent uniformity and conformality. ALD processing is

also extendible to large area substrates and batch processing of multiple substrates. A rich variety of materials can be deposited by ALD including metal oxides, nitrides, fluorides and sulfides, as well as pure elements (7, 8, 12). By alternating between the ALD chemistries for two materials (e.g., a metal and a metal oxide), we can synthesize nanostructured composite coating. The thickness of the coating is controlled by the total number of ALD cycles performed, and the composition is dictated by the relative ratio of the ALD cycles executed for the two components (1, 3).

In this study, we used *in-situ* quartz crystal microbalance (QCM) measurements and mass spectrometry to understand the ALD growth mechanism for composite films comprised of both Mo:Al₂O₃ and W:Al₂O₃. These films were prepared using alternating exposures to trimethyl aluminum (TMA) and H₂O for the Al₂O₃ ALD (7, 8), and alternating MF₆/Si₂H₆ exposures for the metal ALD, where M=Mo or W (8-12). In the case of M:Al₂O₃ films, QCM showed that the metal ALD inhibits the Al₂O₃ ALD and vice versa. Despite this inhibition, the relationship between metal content and ALD metal cycle percentage was easily controlled (1-3). X-ray photoelectron spectroscopy (XPS) elemental analysis showed that the M:Al₂O₃ films are uniform in composition and contain Al, O, and metallic Mo or W as expected, but also include significant F and C. The as-grown composite films were uniform and smooth and had an amorphous microstructure as confirmed by scanning electron microscopy (SEM), atomic force microscopy (AFM) and x-ray diffraction (XRD). Cross-sectional transmission electron microscopy (TEM) revealed the film microstructure to be metallic nanoparticles embedded in an amorphous Al₂O₃ matrix. We have exploited these nanocomposite coatings to functionalize capillary glass array plates to fabricate large-area microchannel plates (MCPs), electron-optic MEMS devices, ceramics electron optics, voltage divider grid structures, etc. The performance of these nanocomposite resistance layer functionalized devices were rigorously investigated and shown excellent results that bode well for the commercialization of these applications.

Experimental

ALD of the Mo:Al₂O₃ and W:Al₂O₃ composite films was performed at 200°C in a hot-walled viscous flow ALD reactor (1, 3). This reactor was equipped with a QCM that allowed *in-situ* studies of the ALD processes. The ultrahigh purity (99.999%) N₂ carrier gas flow was set to 300 sccm, which provided a background base pressure of 1.0 Torr in the ALD reaction chamber as measured by a heated Baratron pressure gauge (MKS model 629B). Details of the ALD experimental conditions are given in Table 1. These conditions for the Al₂O₃, Mo, and W ALD provided self-limiting growth as verified by *in-situ* QCM measurements.

TABLE I. ALD experimental conditions for Mo:Al₂O₃ and W:Al₂O₃ composite film

Parameters	Mo:Al ₂ O ₃	W:Al ₂ O ₃
ALD Precursors	TMA/H ₂ O, MoF ₆ /Si ₂ H ₆	TMA/H ₂ O, WF ₆ /Si ₂ H ₆
Al ₂ O ₃ ALD precursor cycle	TMA-N ₂ purge-H ₂ O-N ₂ purge	TMA-N ₂ purge-H ₂ O-N ₂ purge
Al ₂ O ₃ ALD cycle timings	(1-5-1-5)s	(1-5-1-5)s
Metal ALD precursor cycle	MoF ₆ -N ₂ purge-Si ₂ H ₆ -N ₂ purge	WF ₆ -N ₂ purge-Si ₂ H ₆ -N ₂ purge
Metal ALD cycle timings	(1-5-1-5)s	(1-5-1-5)s
Al ₂ O ₃ precursor vapor pressures	TMA=0.3Torr, H ₂ O=0.2 Torr	TMA=0.3Torr, H ₂ O=0.2 Torr
Metal precursor vapor pressures	Si ₂ H ₆ = 0.25Torr, MoF ₆ =50mTorr	Si ₂ H ₆ = 0.25Torr, WF ₆ =50mTorr

In-situ QCM was performed to examine the growth of Mo:Al₂O₃ and W:Al₂O₃ composite films using different ALD pulse sequences and varying the metal to Al₂O₃ ALD cycle ratio. These QCM measurements typically used 10s N₂ purge times to allow the QCM signal to stabilize after each precursor exposure. TEM analysis was performed by Evans Analytical Group (Sunnyvale, CA). Cross-section TEM samples were prepared using the *in-situ* focused ion beam (FIB) lift out technique on an FEI Strata Dual Beam FIB/SEM. The samples were capped with a protective layer of carbon prior to FIB milling, and were imaged with a FEI Tecnai TF-20 FEG/TEM operated at 200 kV in bright-field (BF) TEM mode, high-resolution (HR) TEM mode, and nano-beam diffraction (NBD) mode. The composition of the Mo:Al₂O₃ and W:Al₂O₃ composite layers was determined by depth profiling using XPS (Evans Analytical Group) and Rutherford backscattering spectroscopy (RBS, Evans Analytical Group). The metal content in the composite films was measured using X-ray fluorescence (XRF, Oxford ED2000). The transvers and lateral resistance of the Mo:Al₂O₃ and W:Al₂O₃ composite layers were determined by performing current-voltage (I-V) measurements on Pt electrode comb structures using a Keithley Model 6487 current-voltage source capable of measuring pico-ammeter current.

Results and Discussion

ALD Cycle Approach for M:Al₂O₃ Composite Films (M = Mo or W)

There are numerous ways to execute ALD precursor dose cycling. For example, Figure 1 shows a representation of one of the of the ALD precursor dosing strategies used to synthesized the M:Al₂O₃ composite films. Alternating TMA/H₂O exposures are executed to deposit the Al₂O₃ component, and periodically one or more Si₂H₆/MF₆ cycles are performed to introduce the Metal component. We define the metal cycle percentage as: $\%M = nM / (nM + mAl_2O_3) * 100$ where nM and mAl₂O₃ are the relative numbers of TMA/H₂O and Si₂H₆/MF₆ cycles performed, respectively. Because of the drastically different bulk resistivities for these materials in their pure form ($\sim 10^{16}$ for Al₂O₃ and $\sim 10^{-4}$ Ohm-cm for ALD Mo or W, respectively), we should be able to tune the resistivity for the M:Al₂O₃ composite layers over a wide range by simply adjusting the %M. Details of individual ALD growth of Mo:Al₂O₃ (3) and W:Al₂O₃ (1) composite material growth have been previously reported.

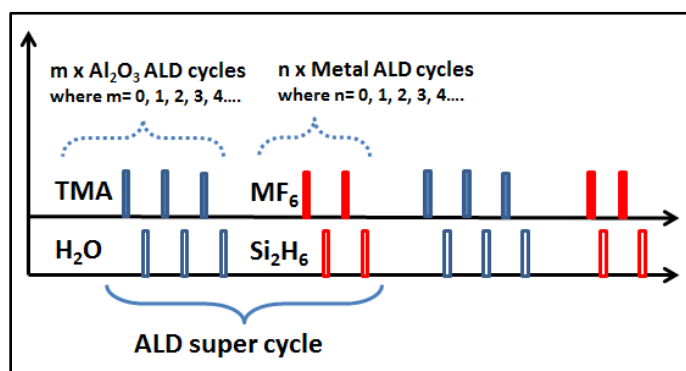


Figure 1. Schematic illustration of ALD cycle precursor pulsing sequence for M:Al₂O₃ nanocomposite coating using alternating TMA/H₂O exposures for the Al₂O₃ ALD and alternating MF₆/Si₂H₆ exposures for the Metal ALD.

QCM Study for M:Al₂O₃ Nanostructured Composite Films (where M = Mo or W)

Here our focus was mainly to understand how the microstructure and electrical properties of the M:Al₂O₃ composite films were influenced by the initial stages of the metal growth on the Al₂O₃ surface and vice versa. The surface chemistries for the individual half-reactions for Al₂O₃, Mo and W have been examined previously (7-12). Figure 2 shows *in-situ* QCM measurements performed during the ALD of pure Al₂O₃, Mo, and W films to quantify the average steady-state mass gains per ALD cycle which are: Al₂O₃ = 35 ng/cm², Mo = 840 ng/cm² and W = 930 ng/cm². From these average mass uptakes and the thickness measured by ellipsometry, we calculated the materials densities to be: 3.0g/cm³, 8.8g/cm³ and 16.7g/cm³ respectively. These thin film materials densities are slightly lower than their corresponding bulk crystalline material densities and this difference can be linked with amorphous growth of Al₂O₃ and nanocrystalline microstructures of the Mo and W.

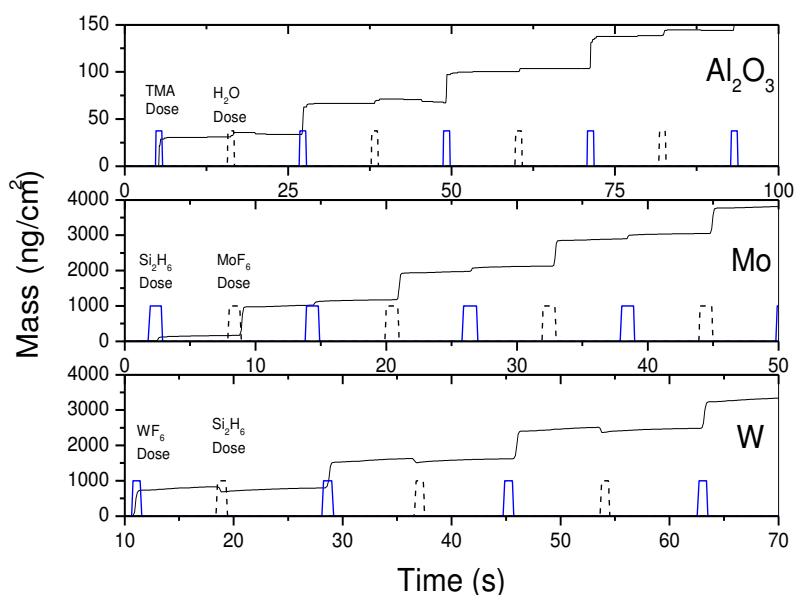


Figure 2. In-situ QCM measurements during the ALD of Al₂O₃, Mo and W in the steady-state growth regime at 200°C

Figure 3 shows *in-situ* QCM measurements performed during the ALD of W on Al₂O₃ (a), Al₂O₃ on W (b), Mo on Al₂O₃ (c) and Al₂O₃ on Mo (d). Clearly, in all cases the mass uptakes are drastically reduced during the initial ALD cycles, and this reflects inhibited nucleation of the metals on Al₂O₃ and vice versa. It is well known that Al₂O₃ ALD is mediated by surface hydroxyl (OH) groups (5), while W ALD occurs via the sacrificial exchange of Si by W where the surface is partially F-terminated after both half-reactions (8-12). In contrast, the reaction of TMA with surface F species is unknown. In addition to this, the reactions of Si₂H₆ and WF₆ are modulated by the OH-terminated alumina such that the ALD W growth rate is suppressed for ~10 cycles before it reaches a steady state. It is remarkable to note that the mass add-on for the W ALD on Al₂O₃ is not monotonic and follows a complex pattern. In comparison to the W ALD, the Mo nucleation is also affected by OH-terminated alumina surface but in contrast to W the

Mo nucleation and mass add-on increases monotonically. The Al_2O_3 growth also exhibits a complex behavior on the fluorinated metal surfaces and requires ~ 8 cycles on Mo and ~ 5 cycles on W to reach the steady state mass uptake level. Additionally, we noticed for both metal and Al_2O_3 , the mass-uptake rates are significantly affected by the relative ratio of the mixing ALD cycles. In both circumstances we noticed the significant complex growth when we performed alternate metal and Al_2O_3 (50-50)% ALD case (1). Despite these complexities, the growth of both the Mo: Al_2O_3 and W: Al_2O_3 composite materials was well controlled.

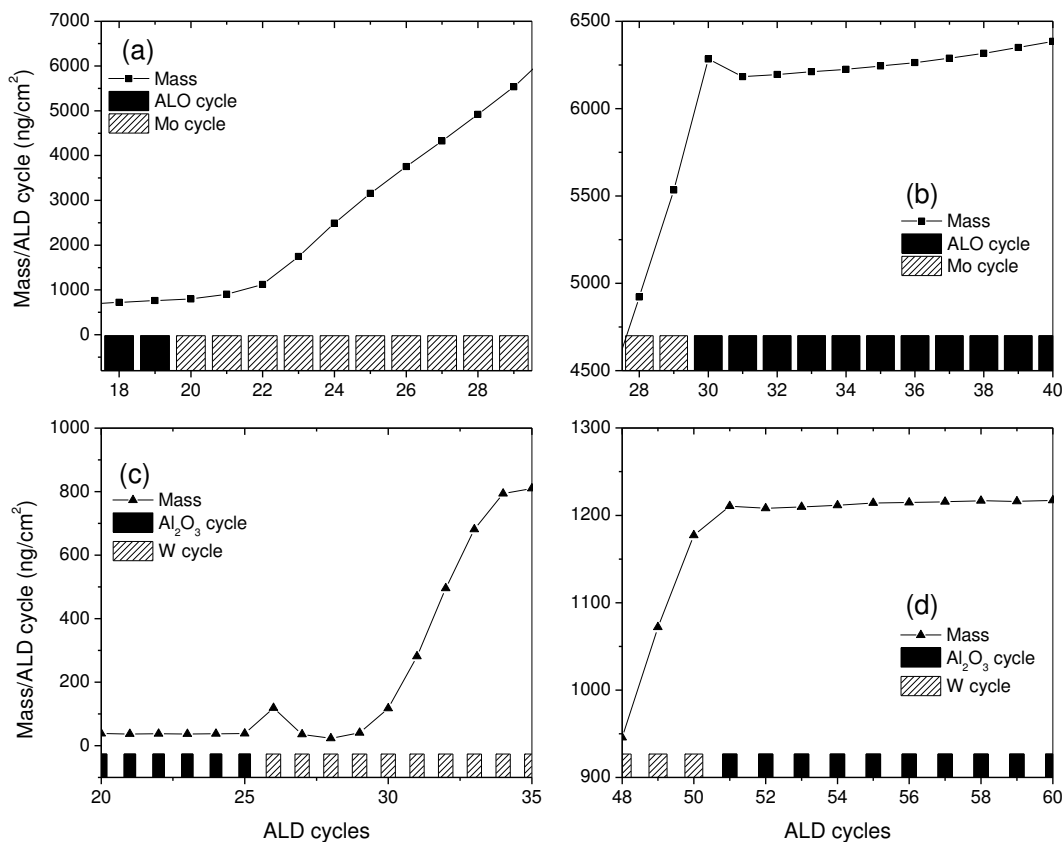


Figure 3. *In-situ* QCM measurements performed during the ALD of: Mo on Al_2O_3 (a) Al_2O_3 on Mo (b), W on Al_2O_3 (c) and Al_2O_3 on W (d).

In comparison to individual growth of metal (W or Mo) on Al_2O_3 and vice versa, the surface chemistry for W: Al_2O_3 and Mo: Al_2O_3 composites ALD are likely complex due to unique reactions that occur during the frequent transitions between the two materials. As examples, Figure 4 shows *in-situ* QCM measurements performed during the ALD of 10%Mo:90% Al_2O_3 (Figures 4a and 4b) and 20%W:70% Al_2O_3 (Figures 4c and 4d) composite layers. A dramatic decrease in the mass uptakes take place compared to the pure Al_2O_3 , Mo, and W steady state mass uptakes, indicating a significant nucleation delay for the metal (W or Mo) on Al_2O_3 and vice versa. This decreased mass uptake can affect the microstructure and electrical properties of the composite materials. These quantities are also strongly dependent on the nature of the ALD super cycles as shown in Figure 1.

Figures 4 a,d show a detailed recording of the QCM signals during the growth of a 10%Mo:90% Al_2O_3 composite film. The TMA, H_2O , Si_2H_6 , and MoF_6 dose times are indicated at the Figure 4b. E.g. between around ALD cycles 25 and 26, two TMA/ H_2O cycles for Al_2O_3 ALD are shown and the QCM signals match the expected mass step pattern for Al_2O_3 ALD. The net mass gain for each Al_2O_3 ALD cycle is $\sim 30 \text{ ng/cm}^2$, which is slightly smaller than the expected value. In contrast, the QCM signals observed during the $\text{Si}_2\text{H}_6/\text{MoF}_6$ exposures do not follow the pattern as shown in Figure 2. In particular, the net mass gain is only $\sim 250 \text{ ng/cm}^2$, which is far below the pure Mo mass steps $= 840 \text{ ng/cm}^2$ and clearly indicates inhibited metal growth.

The QCM measurements recorded during the growth of a 20%W:70% Al_2O_3 film is shown in Figures 4b,d. Al_2O_3 ALD is shown and the QCM signals did not match the expected pattern for Al_2O_3 ALD as shown in Figure 2. The net mass gain for each Al_2O_3 ALD cycle is $\sim 19 \text{ ng/cm}^2$, which is \sim half than the expected value from Al_2O_3 cycle. In contrast, the QCM signals observed during the $\text{Si}_2\text{H}_6/\text{WF}_6$ exposures do not follow the pattern reported in the literature for W ALD as shown in Figure 2. Further the net mass gain is only $\sim 130 \text{ ng/cm}^2$, which is far below the 930 ng/cm^2 expected value for W ALD cause by inhibited nucleation.

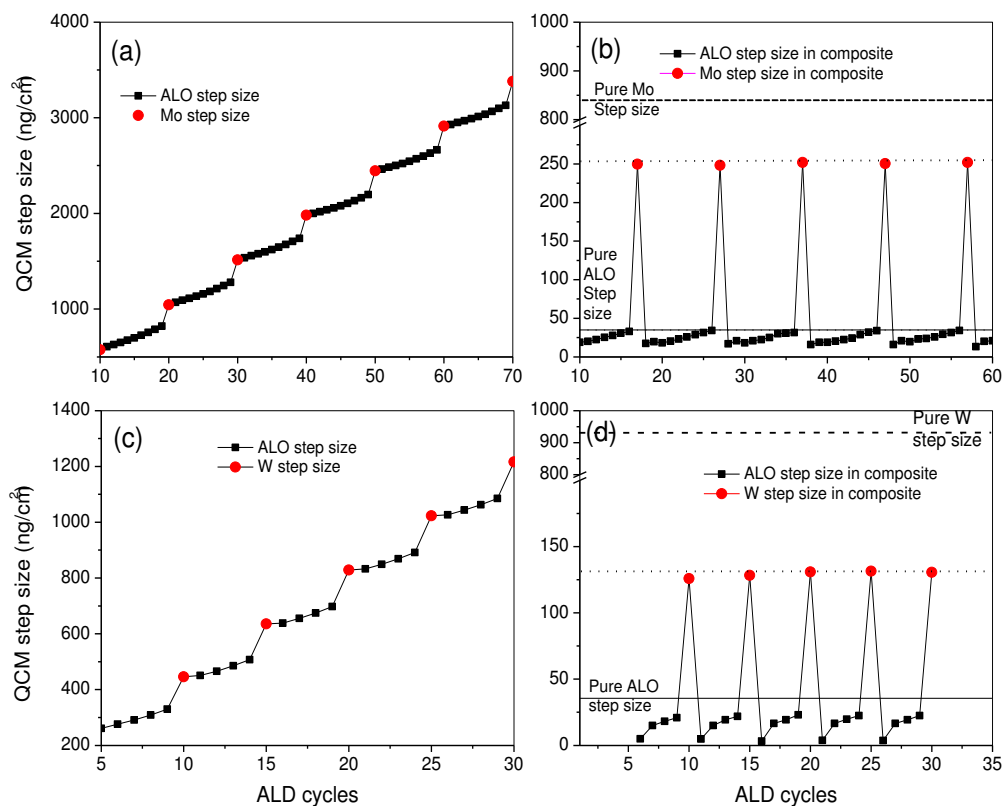


Figure 4. *In-situ* QCM measurements performed during the ALD of: (A) 10%Mo:90% Al_2O_3 : Mass changes produced (4b) by individual ALD cycles as calculated from (4a). The thin solid line at 35 ng/cm^2 and dashed line at 840 ng/cm^2 indicate the average steady-state mass per cycle values for pure Al_2O_3 and Mo ALD, respectively. (B) 20%W:70% Al_2O_3 : where the composite layers mass changes produced (4d) by individual ALD cycles are calculated from Figure (4c). The thin solid line at 35 ng/cm^2 and dashed line at 930 ng/cm^2 indicate the average steady-state mass per cycle values for pure Al_2O_3 and W, respectively.

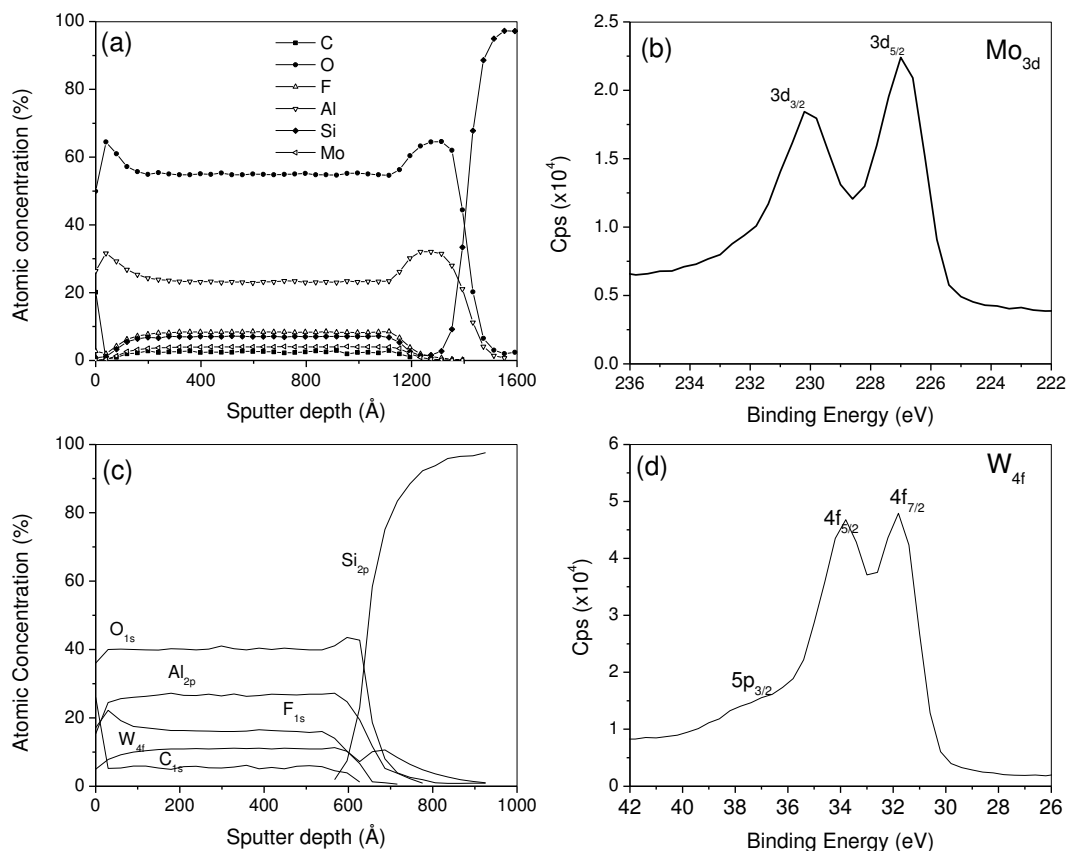
Composition of M:Al₂O₃ Composite Films (where M = Mo or W)

Figure 5: XPS measurements of ALD: (I) 10%Mo:90% Al₂O₃ composite film on Si substrates. Depth profiling measurements showing Al, O, C, and F in the W:Al₂O₃ composite film (a). XPS spectrum of the Mo 3*d* spectral region confirmed the characteristic peaks for metallic Mo (b). (II) 30%W:70% Al₂O₃ composite film deposited on Si substrates. Depth profiling measurements showing Al, O, C, and F in the W:Al₂O₃ composite film (c). XPS scan through W 4*f* spectral region showing characteristic peaks of metallic W (d).

The composition of the Mo:Al₂O₃ and W:Al₂O₃ composite films was determined using XPS depth profiling and RBS measurements of films prepared on Si(100) substrates. These XPS measurements (Figure 5a) of 10%Mo:90% Al₂O₃ revealed that the films contained Al, O, and Mo as expected, but also contained ~5% C and ~10% F. XPS demonstrated that the Mo exists in both the metallic and sub-oxide (Mo⁺⁴) states in the film (Figure 5b). These findings, when combined with the QCM and FTIR measurements, suggest that the TMA reduces the adsorbed MoOF_x species to form AlF₃ and metallic Mo (11). In addition, the C and F presence in the films is similar to that in a previous study which concluded that alternating exposures to niobium pentafluoride and TMA produced films comprised of NbF_x, NbC, C, and AlF₃ (13).

XPS depth profiling of a 30%W:70% Al₂O₃ film was performed and the results are shown in (Figure 5c). The overall elemental composition of the W:Al₂O₃ composite layer is uniform across the film thickness. Figure 5d shows that the composite layer is composed of O, Al, F, W, and C. Based on the surface chemistries for the ALD Al₂O₃ and ALD W in the composite layers, the presence of F and C is unexpected and likely

originates from the unique chemistry that occurs upon transitioning between the W and Al₂O₃ ALD process. As noted above, alternating cycles of niobium NbF₅ and TMA yield films comprised of NbF_x, NbC, C, and AlF₃ (13). The W 4f spectral region (Figure 5d) shows peaks at 31.8 and 33.8 eV characteristic of metallic W and only a weak shoulder at ~37 eV indicating minimal WO_x. From the XPS data, we conclude that the W is mostly metallic in the composite films. The XPS depth profiling measurements yielded sample thickness of 1080Å and 650Å in fair agreement with the thickness of 1210Å and 725Å determined by the spectroscopic ellipsometry for the Mo:Al₂O₃ and W:Al₂O₃ respectively.

Electrical properties of M:Al₂O₃ Composite Films (where M = Mo or W)

Next, a series of Mo:Al₂O₃ and W:Al₂O₃ composite films was prepared on Si(100) substrates using different metal cycle percentages and subsequently studied using current-voltage measurements on comb structures in order to extract the resistivity. Figure 6a shows that the resistivity of the Mo:Al₂O₃ composite films can be tuned over a very broad, 6-decades range (10¹¹-10⁴) by adjusting the Mo cycle percentage from ~7-15%. Figure 6b shows the effect of varying the W cycle percentage on the resistivity. The resistivity decreases approximately exponentially from ~10¹² Ohm-cm at 10 % W cycles to ~10⁸ Ohm-cm at 30% W cycles. This behavior is similar to that of the Mo:Al₂O₃ composite films (Figure 6a), although the slope is much steeper in the case of the Mo:Al₂O₃ composite films (6 decades over 4% change in Mo cycles) as compared to the W:Al₂O₃ composite films (4 decades over 20% change in W cycles). This difference may stem from the much higher deposition rate for the ALD Mo (~10 Å/cycle) versus the ALD W (~5 Å/cycle) under similar growth conditions, especially in light of the exponential relationship between resistivity and metal content. The range of resistivity values provided by these coatings (~10⁴-10¹⁰ Ohm-cm) is particularly useful for applications in electron multipliers (2, 3) and charge drain coatings (3, 14, 15).

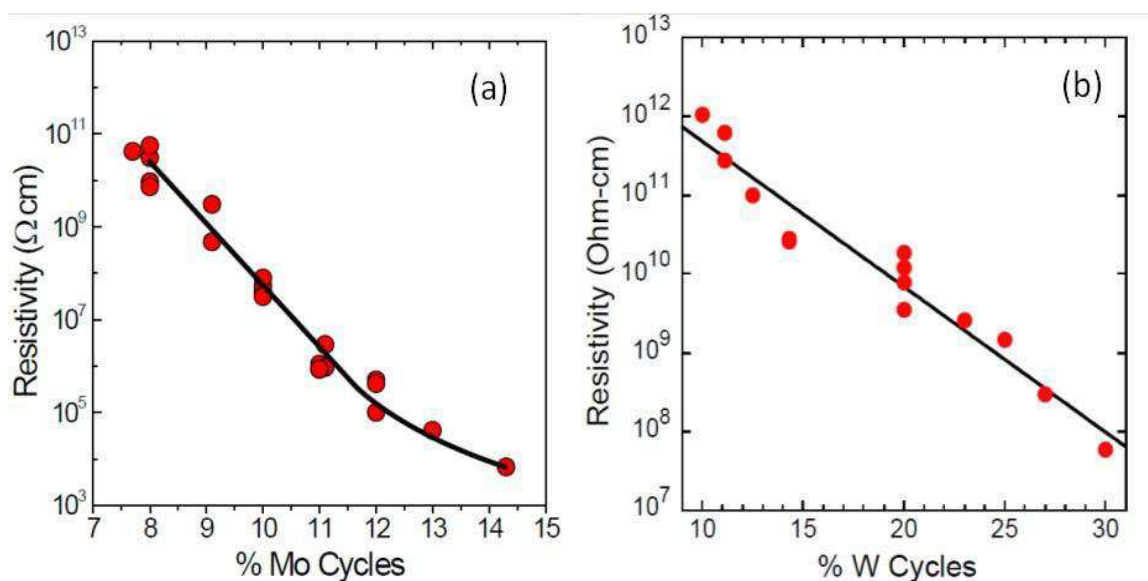


Figure 6: Resistivity of ALD Mo:Al₂O₃ (a) and W:Al₂O₃ (b) composite films as determined by current-voltage measurements versus metal cycle percentage.

Microstructure and Electrical Study for M:Al₂O₃ Composite Films (where M = Mo or W)

In comparison with W growth on Al₂O₃ (Figure 4c), the mass uptake for the Mo growth on Al₂O₃ (Figure 4a) increases monotonically and smoothly with the number of ALD Mo cycles, especially in the early nucleation regime of the first 1-3 ALD cycles. We explored this regime of early nucleation in order to link the microstructural evolution of the films with the accompanying electrical properties. For these studies, we prepared films using the combinations (m, n) = (9:1), (18:2) and (27:3), yielding super cycles comprised of 10, 20 and 30 sub-cycles, respectively. To maintain a nearly constant film thickness, these super cycles were repeated 30, 15, 10 times, respectively so that each film used a total of 300 ALD sub-cycles. These samples were analyzed by high resolution TEM. Figure 7 displays the cross-section TEM images of the Mo:Al₂O₃ composites grown with ALD cycles (Al₂O₃, Mo) = (9, 1) in the top three images, (18, 2) in the middle three images and (27, 3) in the bottom three images. High resolution cross-sectional TEM images were acquired it include the substrate-film interface of Mo:Al₂O₃ composite layer on Si(100). A nano-beam diffraction (NBD) measurement acquired from the composite film (left column). Top-down TEM image of Mo:Al₂O₃ composite film is comprised of nanoparticles (dark spots) embedded in an amorphous matrix. The interface between the Si substrate and the Mo:Al₂O₃ composite film shows an amorphous region attributed to the Si native oxide and the initial Al₂O₃ ALD cycles.

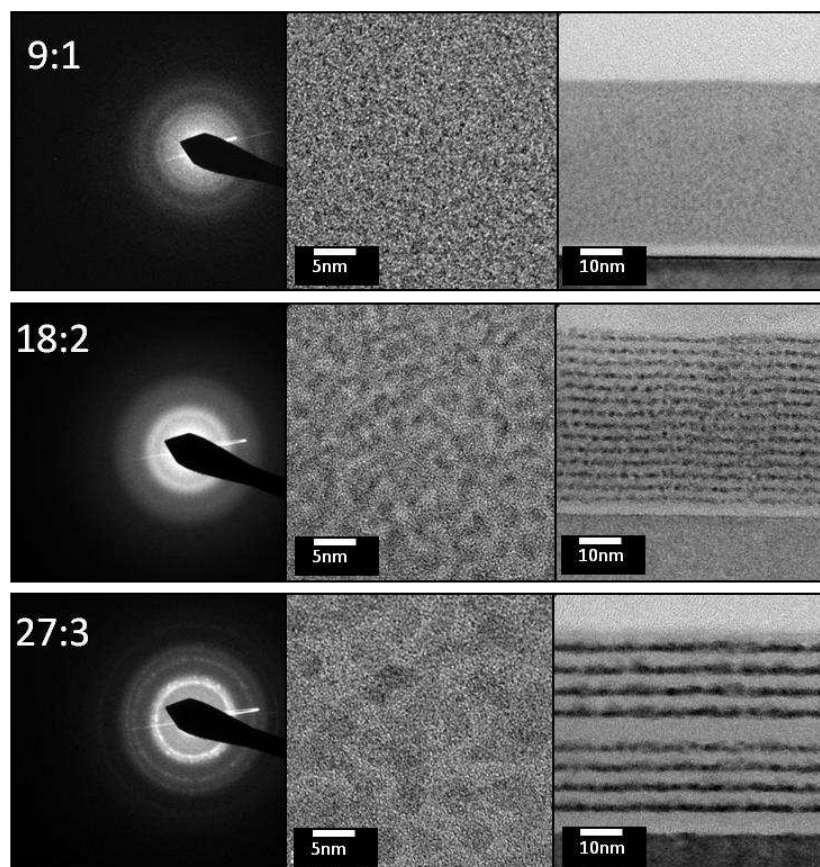


Figure 7: TEM analysis of Mo:Al₂O₃ composite films grown with (Al₂O₃, Mo) = (9:1), (18:2) and (27:3). A nano-beam diffraction (NBD) measurement acquired from the composite film (left column). Top-down TEM image of Mo:Al₂O₃ composite film (middle column). Higher resolution cross-sectional TEM image including the substrate-film interface of Mo:Al₂O₃ composite layer on Si(100).

It is clear that for the (9:1) ALD cycle case, the composite layer is essentially an homogenous blend of ~1nm metal nanoparticles in both the planar and cross-sectional views so that no discrete layers attributable to the super cycles are visible in these films. These metal particles are crystalline as evidenced by the diffuse ring pattern in the selected area diffraction. In contrast, the layer prepared using (18:2) shows a distinct separation between the individual Al₂O₃ and Mo layers. As expected for 18 ALD cycles of TMA/H₂O, the Al₂O₃ layer appears continuous and shows a thickness of ~2 nm. However, the Mo layer is ~1 nm thick and is discontinuous and comprised of larger ~3-4 nm particles as seen in plan view. Likewise, the (27:3) sample also shows distinct layers in cross-section, and the Al₂O₃ thickness is close to the expected value of ~4 nm. In this case, the Mo layer is also continuous and shows an average thickness of ~2 nm. These average thickness values are in-line with the QCM mass uptake measurements for Mo on Al₂O₃ and vice versa. The plan view TEM image for the (27:3) sample shows ~5-7nm Mo particles and the diffraction pattern shows more distinct rings and some speckle attributable to individual Mo nanoparticles within the TEM beam.

Next, the electrical resistivity of these Mo:Al₂O₃ composite films was evaluated using current-voltage measurements with an electrical probe station of films deposited on comb structures for lateral resistivity (Figure 8a) and Hg-probe measurements of films deposited on metal substrates for transverse resistivity (Figure 8b). Note that the electrical transport mechanism in Mo:Al₂O₃ composite layers was previously shown to be Frenkel-Pool emission (14). The transverse and longitudinal resistivity values are comparable for the (9:1) sample, and this finding is consistent with the homogenous and isotropic structure seen by TEM. In contrast, the (18:2) sample shows a remarkable drop in lateral resistivity by approximately 10³ while the transverse resistivity is nearly the same as for the (9:1) sample. We attribute this drop in resistivity to the formation of continuous Mo layers resulting from executing 2 Mo cycles in succession. These continuous layers, which are clearly visible in the TEM cross sectional image, provide a high electrical conductivity in the in-plane direction. In contrast, the transverse resistivity is not affected nearly as much by the continuous Mo sheets since the current must still pass through the ~2 nm insulating Al₂O₃ layers.

The (27:3) sample continues this trend and shows an additional 10x decrease in transverse resistivity compared to the (18:2) sample. This decrease can be attributed to the formation of thicker Mo layer with better connectivity in the lateral direction. It is interesting to note that the transverse resistivity of the (27:3) sample is *increased* by 10x than the (18:2) sample. This may be caused by the higher potential barrier imposed by the thicker ~3nm Al₂O₃ layers. This metal-metal oxide multilayered structure can be thought of as a capacitors stack in which current flow is inhibited and requires a very high breakdown field (12).

We utilized these nanocomposite coatings to functionalize capillary glass array plates to fabricate large-area MCPs suitable for application in large-area photodetectors (2, 3, 13). In addition, we have applied these films as charge drain coatings in MEMS devices for a prototype electron beam lithography tool, and obtained high resolution electron beam patterns without charging artifacts (11, 14).

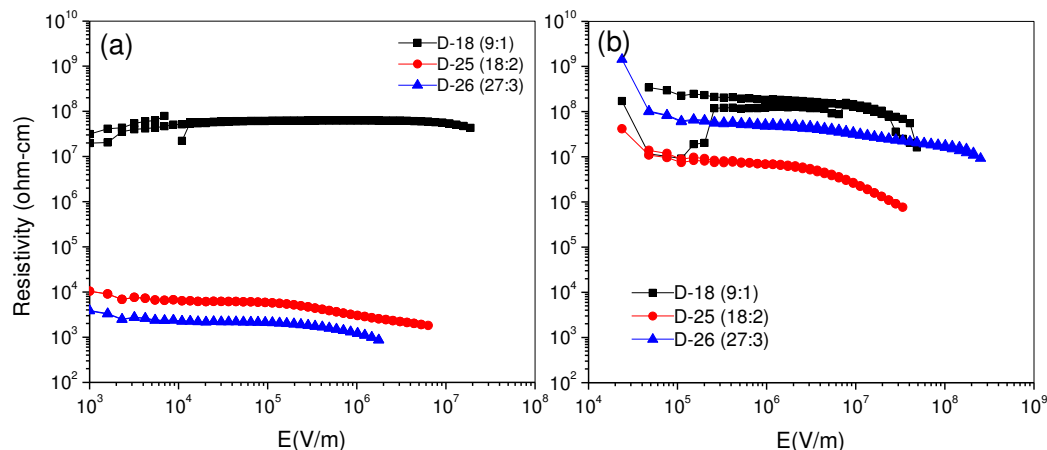


Figure 8: Resistivity versus applied electric field for ALD Mo:Al₂O₃ composite films prepared using (Al₂O₃, Mo) = (9:1), (18:2) and (27:3) measured in the lateral direction on comb structures (a) and in the transverse direction on MIM structures by Hg probe (b).

Conclusions

We have developed nanocomposite coatings consisting of conducting, metallic nanoparticles embedded in an amorphous dielectric matrix. These films are comprised of M:Al₂O₃ where M= W or Mo, and are prepared by ALD using alternating exposures to TMA and H₂O for the Al₂O₃ ALD, and alternating MF₆/Si₂H₆ exposures for the metal ALD. By varying the ratio of ALD cycles for the metal and the Al₂O₃ components in the film, we can tune precisely the resistance of these coatings over a very broad range from 10⁵-10¹² Ohm-cm. We employed *in-situ* QCM to understand the ALD growth mechanism for the M:Al₂O₃ nanocomposite films. Cross-sectional TEM revealed the film structure to be metallic nanoparticles embedded in an amorphous matrix. By adjusting the ALD cycles sequencing we have tailored the microstructure and electrical properties.

Acknowledgements

This work was supported by the U.S. Department of Energy, Office of Science, Office of Basic Energy Sciences and Office of High Energy Physics under contract DE-AC02-06CH11357 as part of the Large Area Picosecond Photodetector (LAPPD) project. The work at KLA-Tencor was partly sponsored by Defense Advanced Research Projects Agency under contract number HR0011-07-9-0007. The views, opinions, and/or findings contained in this article/presentation are those of the author/presenter and should not be interpreted as representing the official views or policies, either expressed or implied, of the Defense Advanced Research Projects Agency or the Department of Defense.

References

- 1 A. U. Mane and J. W. Elam, *Chemical Vapor Deposition*, **19**, 4-6, 186, (2013).
- 2 A. U. Mane, Q. Peng, J. W. Elam, D. C. Bennis, C. A. Craven, M. A. Detarando, J. R. Escolas, H. J. Frisch, S. J. Jokela, J. McPhate, M. J. Minot, O. H. W. Siegmund, J. M. Renaud, R. G. Wagner, and M. J. Wetstein, 2012, "An atomic layer deposition method to fabricate economical and robust large area microchannel plates for photodetectors", in *Proceedings of the 2nd International Conference on Technology and Instrumentation in Particle Physics*, edited by T. Liu, Vol. 37, pp. 722.
- 3 J. W. Elam, 2012, "Coatings on High Aspect Ratio Structures", in *Atomic Layer Deposition of Nanostructured Materials*, edited by N. Pinna and M. Knez (Wiley-VCH, Weinheim), pp. 227.
- 4 O. H. W. Siegmund, J. McPhate, A. S. Tremsin, S. R. Jelinsky, H. J. Frisch, J. W. Elam, A. U. Mane, R. G. Wagner, M. J. Minot, J. M. Renaud, and M. A. Detarando, *Physics Procedia*, **37**, 803, (2012).
- 5 A. Brodie, P. De Cecco, C. Bevis, J. R. Maldonado, R. Bhatia, E. Deguns, and G. Sundaram, 2010, "Fabrication of Coatings with Targeted Tunable Electrical Properties via ALD: Al₂O₃/ZnO and Nb₂O₅/Ta₂O₅", in *Atomic Layer Deposition Applications 6*, edited by J. W. Elam, S. DeGendt, O. VanDerStraten, A. Delabie, A. Londergan, S. F. Bent, and F. Roozeboom, Vol. 33, pp. 101.
- 6 D. R. Beaulieu, D. Gorelikov, H. Klotzsch, P. de Rouffignac, K. Saadatmand, K. Stenton, N. Sullivan, and A. S. Tremsin, *Nuclear Instruments & Methods in Physics Research Section a-Accelerators Spectrometers Detectors and Associated Equipment*, **633**, S59, (2011).
- 7 S. M. George, *Chemical Reviews*, **110**, 1, 111, (2010).
- 8 J. W. Elam and S. M. George, *Chemistry of Materials*, **15**, 1020, (2003).
- 9 J. W. Elam, D. Routkevitch, and S. M. George, *Journal of the Electrochemical Society*, **150**, 6, G339, (2003).
- 10 J. D. Ferguson, A. W. Weimer, and S. M. George, *Applied Surface Science*, **162-163**, 280, (2000).
- 11 D. Seghete, G. B. Rayner, Jr., A. S. Cavanagh, V. R. Anderson, and S. M. George, *Chemistry of Materials*, **23**, 7, 1668, (2011).
- 12 F. H. Fabreguette, Z. A. Sechrist, J. W. Elam, and S. M. George, *Thin Solid Films*, **488**, 1-2, 103, (2005).
- 13 J. A. Klug, T. Proslie, J. W. Elam, R. E. Cook, J. M. Hiller, H. Claus, N. G. Becker, and M. J. Pellin, *Journal of Physical Chemistry C*, **115**, 50, 25063, (2011).
- 14 W. M. Tong, A. D. Brodie, A. U. Mane, S. Fuge, F. Kidwingira, M. A. McCord, C. F. Bevis, and J. W. Elam, *Applied Physics Letters*, **102**, 25, 252901 (5 pp.), (2013).
- 15 P. Petric, C. Bevis, M. McCord, A. Carroll, A. Brodie, U. Ummethala, L. Grella, A. Cheung, and R. Freed, *Journal of Vacuum Science & Technology B*, **28**, 6, C6C6, (2010).